Room Temperature Crystal Structure, Magnetic and Dielectric Behaviour of $(1-x)BiFeO_3$-$xSr(Fe_{0.5}Nb_{0.5})O_3$ Solid Solution $(0.1 \leq x \leq 1.0)$

4.1 Introduction

As discussed in Chapter 1, due to attractive multiferroic properties, $BiFeO_3$ has the potential for designing multifunctional devices such as spintronic, actuator, sensor and data storage applications [Ramesh and Spaldin (2007), Eerenstein et al. (2006), Fiebig (2005)]. However, long period modulated magnetic cycloidal structure of periodicity 62nm [Sosnowaska et al. (1982)] inhibits linear magnetoelectric response with zero net macroscopic magnetization in $BiFeO_3$ [Popov et al. (2001)]. To release the latent magnetization and to observe magnetoelectric response, it is necessary to destroy the magnetic cycloid in $BiFeO_3$ [Singh et al. (2011)]. As explained in chapter 1, there are number of ways to destroy the magnetic cycloid of $BiFeO_3$ like, reduction of particle size below the periodicity ($\sim$ 62nm) of magnetic cycloid of $BiFeO_3$ [Park et al. (2007)], transformation of the spatially modulated spin cycloid to a spatially uniform antiferromagnetic structure by applying very strong magnetic field (greater than 18-20 Tesla) [Popov et al. (1993), Ruette et al. (2004)], thin films formation with epitaxial strains [Eerenstein et al. (2005)], and substitution of isovalent/heterovalent ions on Bi and/or Fe-sites [Sosnowska et al. (2002), Sosnowska et al. (1996), Wang et al. (2012), Itoh et al. (2009)]. Among these methods, the most convenient and easy way to destroy the magnetic cycloid of $BiFeO_3$ is the preparation of solid solution of $BiFeO_3$ with some other perovskite materials such as $LaFeO_3$, $BiMnO_3$, $BaTiO_3$, $CaTiO_3$, $SrTiO_3$ and $Pb(Fe_{0.5}Nb_{0.5})O_3$ [Sosnowska et al. (2002), Sosnowska et al. (1996), Wang et al. (2012), Itoh et al. (2009), Singh et al. (2008)C, Patel et al. (2013)] leading to the modifications in the effective ionic radii of Bi- and Fe sites. In view of this, we have investigated the new solid solution system $(1-x)BiFeO_3-xSr(Fe_{0.5}Nb_{0.5})O_3$ for crystal structure, dielectric, ferroelectric, magnetic and multiferroic properties on various compositions.

To the best of our knowledge no work has been reported in literatures on the crystal structure and the magnetic properties of the $(1-x)BiFeO_3-xSr(Fe_{0.5}Nb_{0.5})O_3$ [$(1-x)$BF-xSFN)] ceramic system. Since the crystal structure of the two end components are different, ($BiFeO_3$ is rhombohedral ($R3c$ space group) and $Sr(Fe_{0.5}Nb_{0.5})O_3$ is tetragonal ($I4/mcm$ space group)), it will be interesting to investigate how the crystal structure change from rhombohedral to tetragonal on changing compositions. One also expects crystallographic phase coexistence and appearance of new crystal structures on changing composition.

This chapter present the results of a comprehensive study of the room temperature crystal structure of $(1-x)$BF-xSFN solid solution in the entire composition range ($0.1 \leq x \leq 1.0$), using high resolution laboratory X-ray powder diffraction data. Composition dependence of room temperature dielectric permittivity and remnant magnetization (M_r) has been investigated to correlate them with the crystallographic phase transformations. The impact of solid solution formation of SFN on the magnetic properties of $BiFeO_3$ is also investigated by room temperature magnetization (M)-magnetic field (H) hysteresis loop measurements and high temperature magnetization studies on several compositions of the solid solution.

4.2 Experimental

The different compositions of $(1-x)$BF-xSFN samples were synthesized by the solid state ceramic method as discussed in chapter 2. The sintered pellets of different compositions were crushed using an agate mortar and pestle into fine powders. The properly crushed powders were annealed at 773 K for 10 hours to remove strains introduced during crushing. The annealed powders were used to record the X-ray powder diffraction patterns using Rigaku SmartLab high resolution x-ray diffractometer having $CuK\alpha_1$ optics. Absence of $CuK\alpha_2$ component in the diffraction patterns helps in

unambiguous structure determination. The data were recorded in the 2θ range of 20° to 120° at a step of 0.02°. A brief introduction to the Rietveld structure refinement method for detailed structural characterization is discussed in chapter 2. For dielectric measurements, both sides of sintered pellets were cleaned carefully then silver electrode were applied on flat surfaces and fired on at temperature 773K for 5 minutes. The room temperature dielectric permittivity (ε_r) of electroded pellets of various compositions were measured using Nova Control (alpha-A) high performance impedance analyser. The room temperature magnetization versus magnetic field (M-H loop) and temperature dependent dc magnetization M(T) measurements [zero field cooled (ZFC), field cooled cooling (FCC) and field cooled warming (FCW)] in the temperature range 300 K to 800 K at a low magnetic field of 500 Oe were carried out using a Quantum Design MPMS-3 system based on SQUID.

4.3 Details of Rietveld Structure Refinement for (1-x)BF-xSFN) Ceramic

Rietveld refinements of X-ray powder diffraction patterns were carried out using the FULLPROF suite [Carvajal (2010)]. The Wyckoff positions and the asymmetric unit corresponding to the various space groups used during Rietveld refinements of different crystallographic structures observed in (1-x)BF-xSFN system is described below.

(i) For the refinement of rhombohedral structure with the $R3c$ space group, we used hexagonal unit cell axes with the lattice parameters $a_H \approx b_H \approx 2^{1/2}a_{pc}$ and $c_H \approx 2(3^{1/2}) a_{pc}$, where a_{pc} corresponds to the primitive (p_c) (pseudocubic cell) cell parameter. There are three ionic sites (Bi^{3+}/ Sr^{2+}, Fe^{3+}/Nb^{5+} and O^{2-}) in the asymmetric unit of the rhombohedral structure. The Bi^{3+}/ Sr^{2+} and Fe^{3+}/Nb^{5+} ions occupy the 6(a) Wyckoff site at (0, 0, z) while O^{2-} ions at the 18(b) Wyckoff sites at (x, y, z). The coordinates of all the atoms in the asymmetric unit cell of the $R3c$ space group can also be written as a

function of the displacement parameters, s, t, d and e, as per Megaw et al. (1975): Bi^{3+}/ Sr^{2+} (0, 0, 0.25+s), Fe^{3+}/Nb^{5+} (0, 0, t), O^{2-} (0.1666-2e-2d, 0.3333-4d, 0.0833). The parameters 's' and 't' describe the polar displacement of cations Bi^{3+}/ Sr^{2+} and Fe^{3+}/Nb^{5+} along $[001]_{hex.}$. The displacement parameter 'e' of oxygen (O^{2-}) from its ideal cubic position is related to the tilt angle (ω) of anti-phase rotation of the oxygen octahedra about the trigonal $[111]_{rh}$ or $[001]_h$ direction through the expression $\omega = \tan^{-1}(4e\ (3^{1/2}))$. The parameter 'd' is related to the distortion of the BO_6 (B: Fe^{3+}/Nb^{5+}) octahedron.

(ii) The monoclinic phase in the *Cc* space group has one Wyckoff site symmetry 4(a) with general coordinates. The unit cell consists of four formula units of (1-x)BF-xSFN, and asymmetric unit of structure consists of five atoms in which Bi^{3+}/Sr^{2+} are at (0.00, 0.25, 0.00) and Fe^{3+}/Nb^{5+} at (0.25+$\delta x_{Fe/Nb}$, 0.25+$\delta y_{Fe/Nb}$, 0.75+$\delta z_{Fe/Nb}$), while the remaining three oxygen atoms are O1 at (0.00+ δx_{O1}, 0.25+ δy_{O1}, 0.50+ δz_{O1}), O2 at (0.25+ δx_{O2}, 0.50+ δy_{O2}, 0.00+ δz_{O2}) and O3 at (0.25+ δx_{O3}, 0.00+ δy_{O3}, 0.00+ δz_{O3}). Here the symbols $\delta^{,s}$ represent the respective atomic shift. Following the structural model used by Ranjan et al. (2005) for the *Cc* phase of $Pb(Zr_{0.52}Ti_{0.48})O_3$, Bi^{3+}/Sr^{2+} position was kept at (0.00, 0.25, 0.00) to fix the origin during refinement.

(iii) For the cubic phase in the *Pm-3m* space group, there are three ions (Bi^{3+}/Sr^{2+}, Fe^{3+}/Nb^{5+} and O^{2-}) in the asymmetric unit of which Bi^{3+}/ Sr^{2+} ions will occupy the 1(a) Wyckoff site at (0, 0, 0), Fe^{3+}/Nb^{5+} occupy 1(b) Wyckoff site at (0.5, 0.5, 0.5), and O^{2-} occupy 3(c) Wyckoff site at (0.5, 0.5, 0).

(iv) As discussed in chapter 3 also, for Rietveld structure refinement with tetragonal *I4/mcm* space group, the asymmetric unit of structure consists of four atoms in which, Sr occupies the 4b sites at (0.00, 0.50, 0.25) and the Fe/Nb on 4c sites at (0.0, 0.0, 0.0), while the remaining two type of oxygen ions are O(1) on 4a sites at (0.00, 0.0, 0.25) and

O(2) on 8h sites at (0.25+ δ, 0.75+ δ, 0.00). Here the symbol 'δ' represents the refinable shift.

4.4 Results and Discussion

4.4.1 Composition Dependent Crystallographic Phase Transitions in (1-x)BiFeO₃-xSr(Fe₀.₅Nb₀.₅)O₃ Ceramic

To investigate the room temperature crystal structure of (1-x)BiFeO₃-xSr(Fe₀.₅Nb₀.₅)O₃ as a function of composition (x), we first present a qualitative analysis of some selected x-ray powder diffraction profiles for different compositions. Fig. 4.1 shows the XRD profiles of the (111), (200), (220) and (222) (all indices with respect to pseudocubic perovskite cell) reflections (without CuKα_2 contribution) for various compositions of (1-x)BF-xSFN), in the range $0.10 \leq x \leq 1.00$. In the existing literature on BiFeO₃ based solid solutions, the reported crystal structures are rhombohedral in the *R*3*c* space group, monoclinic in the *Cc* space group, cubic in the *Pm*-3*m* space group and tetragonal structure in the *P*4*mm* space group observed in different compositions [Ismailzade et al. (1981); Kumar et al. (2000), Singh et al. (2008C), Bhattacharjee et al. (2010A)]. For the cubic structure with *Pm*-3*m* space group, the (111), (200) and (220) pseudocubic profiles shown in Fig.4.1 have to be singlet. For a rhombohedral structure with *R*3*c* space group, the (200) reflection is a singlet while (111) and (220) are doublets with weaker reflections (11-1) and (2-20) on the lower 2θ side. For the monoclinic structure in *Cc* space group, the reflections (111), (220) and (222) should be multiplet while 200 should be a doublet [Singh et al. (2007)]. With above characteristics of the diffraction profiles for these crystal structures with the *R*3*c*, *Cc*, *P*4*mm* and *Pm*-3*m* space groups, we can proceed to analyze the crystal structures of (1-x)BF-xSFN) from the XRD profiles given in Fig. 4.1. We have already shown in Chapter 3, that the structure of pure SFN (x=1) is tetragonal in the *I*4/*mcm* space group.
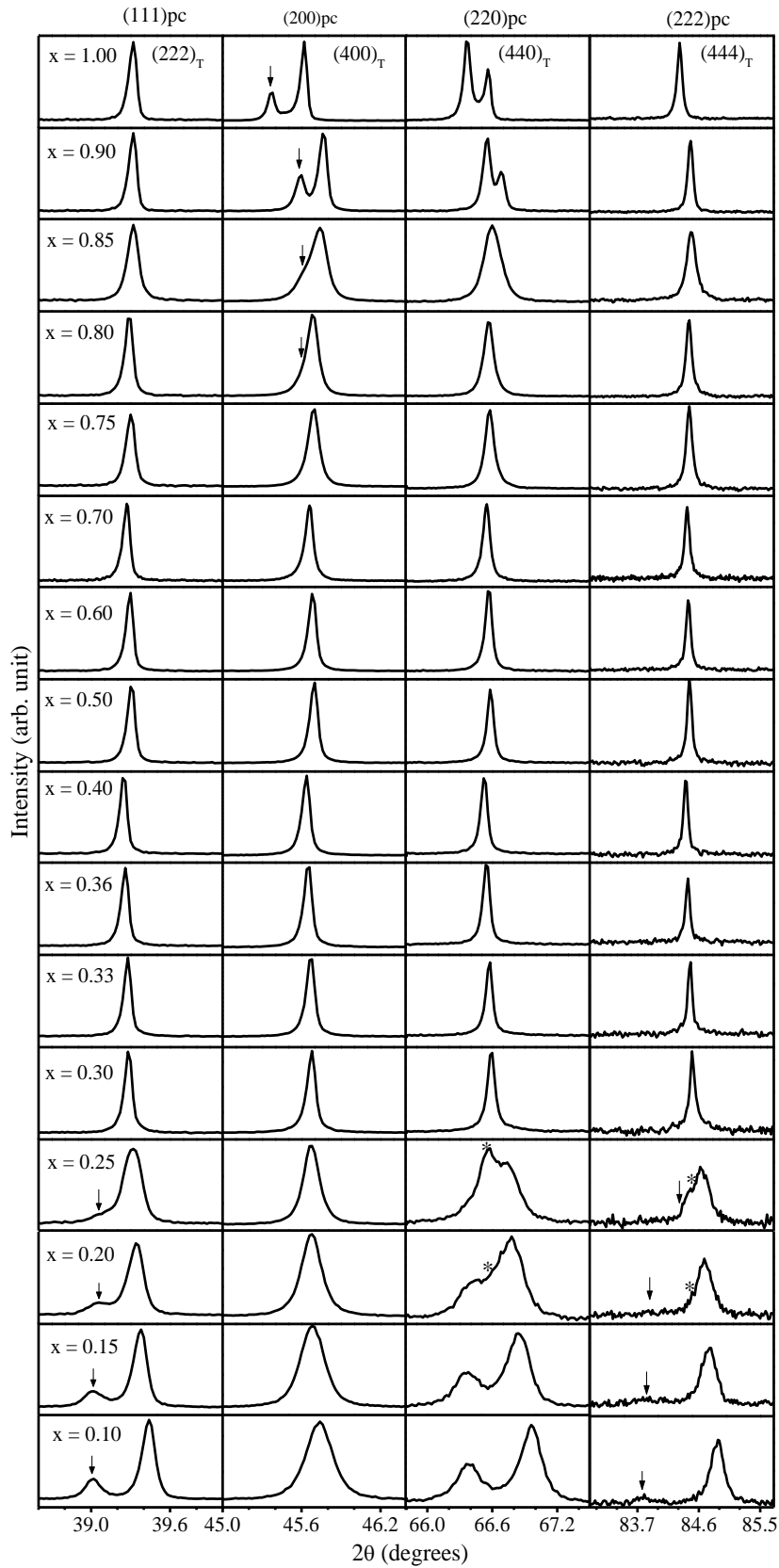
Figure 4.1 Evolution of the x-ray powder diffraction profiles of the pseudocubic (111), (200), (220) and (222) reflections (considering pseudocubic unit cell) as a function of composition for the $(1-x)BiFeO_3-xSr(Fe_{0.5}Nb_{0.5})O_3$ ceramic.

The nature of splitting of the diffraction profiles for tetragonal *P4mm* and *I4/mcm* space groups are similar, except that, the superlattice reflections also appear in the diffraction pattern for the *I4/mcm* space group due to rotation of the oxygen octahedra. As can be seen from Fig.4.1, the compositions close to BiFeO$_3$ end with lower concentration of SFN (x<0.25) exhibit rhombohedral like characteristics showing (111), (220) and (222) as doublets and (200) as singlet. However, a close examination of the diffraction profiles suggests that the (200) is extraordinarily broad and the higher angle peak of the (222) doublet, has extra shoulder like features, corresponding to an additional peak. This is illustrated more clearly in Fig.4.2 (a), which shows the zoomed view of the higher angle peak of the (222) doublet for x=0.10. These observations indicate that the compositions with x<0.25 are not rhombohedral and possibly there is a monoclinic phase which can explain the additional splitting in the XRD profiles. To confirm further the non-rhombohedral structure for the compositions with x<0.25, we show in Fig. 4.2 (b), composition dependent variation of the full width at half maximum (FWHM) ratio of (200) to (111) pseudocubic XRD profiles. For rhombohedral structure, this ratio should be close to one as the two diffraction profiles are not far apart on the two-theta axis. However, as can be seen from Fig. 4.2 (b), for the compositions with x = 0.10 and 0.15, FWHM of 200 peak is nearly 2 times of 111 peak. This clearly rules out the rhombohedral structure for these compositions. As confirmed in the next section from Rietveld structure refinement, the structures of the compositions with x = 0.10 and 0.15 are monoclinic in the Cc space group, similar to that reported in compositions close to BiFeO$_3$ end for (1-x)BiFeO$_3$-xPbTiO$_3$ solid solution [Bhattacharjee and Pandey (2010)A]. As can be seen from Fig.4.1, the monoclinic splitting of the (111) and (220) pseudocubic XRD profiles decreases gradually with increasing concentration of Sr(Fe$_{0.5}$Nb$_{0.5}$)O$_3$ doping (x). A closer look on the middle part of (200) XRD profiles for

the compositions with x= 0.20 and 0.25 suggest the presence of extra intensity due to evolution of probably a new phase coexisting with the primary phase (i. e. monoclinic phase). This extra intensity evolves as a new peak for the composition with x=0.30 with simultaneous disappearance of the side shoulders present in the (200) profiles for the composition with x=0.25. The evolution of this new peak is indicated by * in Fig. 4.1. For the compositions with further higher SFN concentration (x=0.33), all the diffraction profiles shown in Fig.4.1 are singlets, which characterizes the appearance of cubic phase in intermediate compositions. To investigate it further, we show in Fig.4.3, composition dependent evolution of x-ray diffraction pattern in the selected 2θ range of 36.8 to 40.2° and integrated intensity of the strongest superlattice reflection around $2\theta \sim 37.5°$ for different compositions. As can be seen from Fig.4.3, the intensity of the superlattice reflection decreases slowly with increasing SFN concentration and vanishes for x=0.33.
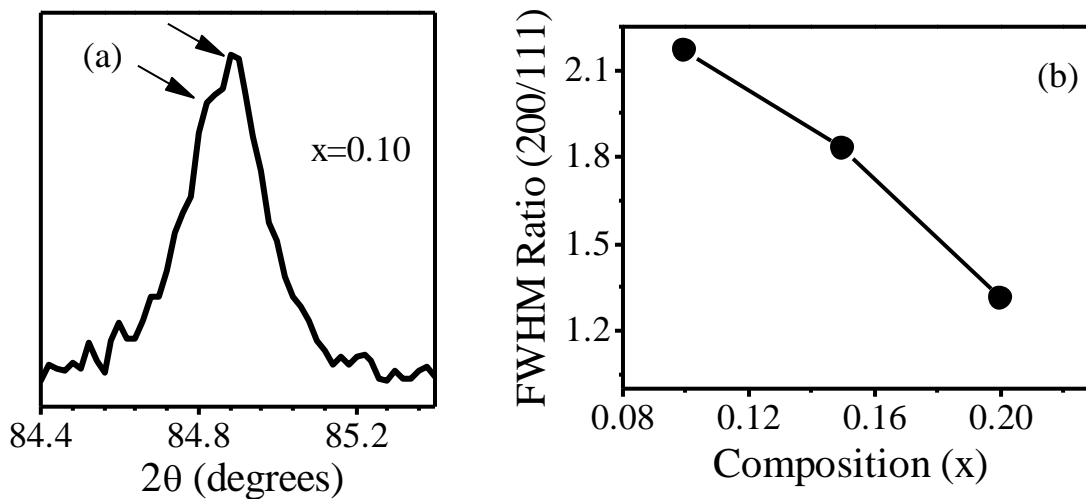

Figure 4.2 (a) A zoomed view of (222) XRD profile for x = 0.10. Arrows indicate the splitting in the XRD profile. (b) Composition dependent variation of the FWHM ratio of (200) to (111) profiles for $(1-x)BiFeO_3-xSr(Fe_{0.5}Nb_{0.5})O_3$ ceramics.
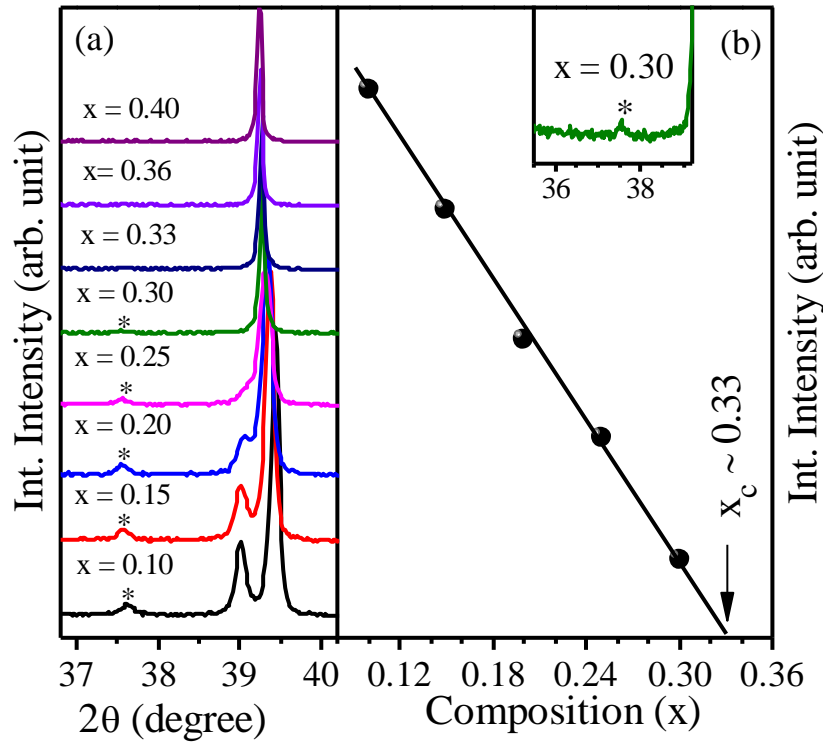
Figure 4.3 Composition dependent variation of (a) x-ray diffraction pattern in the selected 2θ range of 36.8 to 40.2° for various compositions of $(1-x)BiFeO_3$-$xSr(Fe_{0.5}Nb_{0.5})O_3$ ceramic (b) composition dependence of integrated intensity of the strongest superlattice reflection around $2\theta \sim 37.5°$ for $0.10 \leq x \leq 0.30$. Asterisks in (a) indicate the presence of superlattice reflections, while the arrow in (b) indicates the composition at $x_c \sim 0.33$ for crystallographic phase transition. The inset to (b) shows zoomed view of the superlattice reflection for x=0.30.

Even though, all the reflections for x = 0.30 composition seem to be singlet in Fig. 4.1, suggesting a cubic phase, but the appearance of low intensity superlattice reflection (shown in the inset of Fig. 4.3 (b)) suggests that a minor contribution of monoclinic phase is still present. Due to this minor contribution of monoclinic phase the splitting of corresponding peaks are too small to be visualised. It is evident from Fig. 4.3(b) that the integrated intensity decreases linearly with increasing SFN doping (x) and becomes zero for the critical composition $x_c \approx 0.33$. The monoclinic splitting of the pseudocubic reflections such as (111) and (220) are also disappearing completely for the x = 0.33

115

composition. Thus the monoclinic structure of (1-x)BF-xSFN for the compositions with x=0.10 and 0.15 gradually transforms to cubic phase with increasing SFN concentration through a phase coexistence region were both the monoclinic (*Cc*) and cubic (*Pm-3m*) structures coexist. The phase coexistence region is observed for the compositions with $0.20 \leq x \leq 0.30$ having compositional width of $\Delta x \approx 0.10$. The intermediate compositions of (1-x)BF-xSFN ceramic in the compositions range $0.33 \leq x \leq 0.70$ show singlet nature of diffraction profiles (see Fig.4.1), confirming the stability region of cubic structure in the *Pm-3m* space group for these compositions.

To investigate the structure of (1-x)BF-xSFN ceramic with higher SFN concentration (x>0.70), we show in Fig. 4.4, the evolution of x-ray diffraction patterns in the selected 2θ range 34.25 to $42°$ for various compositions ($0.70 \leq x \leq 1.00$). As presented in Chapter 3, the structure of pure SFN (x=1) is tetragonal with *I4/mcm* space group. As can be seen from Fig. 4.4, the intensity of the superlattice reflection (marked by symbol *) appearing around $2\theta \sim 37.5^0$ characterizing the tetragonal phase with I4/mcm space group, gradually decreases with decreasing value of SFN concentration (x) and disappears completely for x = 0.70. This directly indicates the persistence of tetragonal phases up to x = 0.75 composition. Below this composition (x = 0.75), the disappearance of superlattice reflection and singlet nature of peaks indicate the appearance of cubic phase. It is also evident from Fig.4.1, that the tetragonality of (1-x)BF-xSFN ceramic for the compositions close to the SFN end decreases with decreasing (x) and finally transforms to a cubic phase for x=0.70. For x = 1.00 and 0.90, the tetragonal splitting of (200) and (220) peaks are very clear while for x = 0.85, 0.80 only asymmetric tail is seen in the (200) XRD profiles. The tetragonal splitting is barely visible for x= 0.75 but weak superlattice reflection is seen. This suggest that the tetragonal structure is coexisting with the neighbouring cubic structure stable for the

lower SFN compositions (x<0.70). As shown in the next section, the Rietveld structure refinement confirms the coexistence of tetragonal (*I4/mcm*) and cubic (*Pm-3m*) structures for the composition range $0.75 \leq x \leq 0.85$.
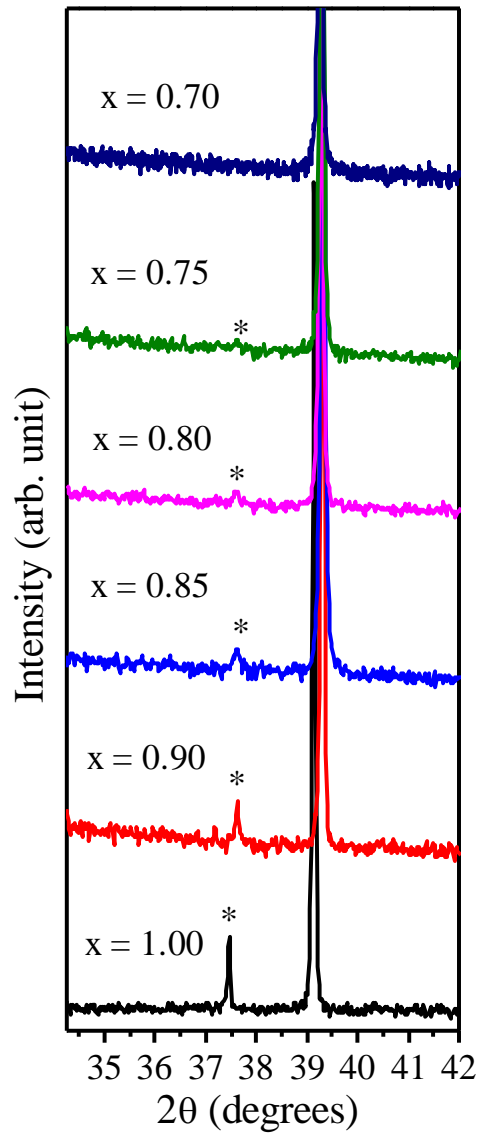

Figure 4.4 Evolution of x-ray diffraction patterns in the selected 2θ range 34.25 to 42° for various compositions of $(1-x)BiFeO_3-xSr(Fe_{0.5}Nb_{0.5})O_3$ ceramic ($0.70 \leq x \leq 1.00$). Asterisks (*) mark the superlattice reflections.

4.4.2 Rietveld Structure Refinement of $(1-x)BiFeO_3$-$xSr(Fe_{0.5}Nb_{0.5})O_3$ for x= 0.10 and 0.15 (Monoclinic Structure with *Cc* space group)

As discussed in the previous section, the structures of the $(1-x)BiFeO_3$-$xBaTiO_3$ compositions with x = 0.10 and 0.15 appear to be monoclinic in the *Cc* space group, similar to that reported in compositions close to $BiFeO_3$ end for $(1-x)BiFeO_3$-$xPbTiO_3$ solid solution [Bhattacharjee and Pandey (2010)A]. To confirm the monoclinic structure with *Cc* space group for the compositions with x=0.10 and 0.15, we performed the Rietveld structural analysis of the x-ray diffraction profiles. As the starting structural model for Rietveld refinement using *Cc* space group, we have taken the lattice parameters and positional coordinates reported for $0.90BiFeO_3$-$0.10PbTiO_3$ [Bhattacharjee and Pandey (2010)A]. The Rietveld refinement of the structure using *Cc* space group gives quite good match between experimental and calculated XRD patterns with acceptable values of agreement factors R_{wp} = 7.72 and χ^2 = 1.88. A very good fit between experimental and calculated XRD patterns obtained from Rietveld structure refinement using monoclinic *Cc* space group for x=0.10 is shown in Fig. 4.5 (a). For completeness, we also performed Rietveld structure refinement for x=0.10 considering rhombohedral model with *R*3*c* space group. The lattice parameters and positional coordinates of pure $BiFeO_3$ were used for the staring structural model. The Rietveld structure refinement using *R*3*c* space group does not give satisfactory fit (R_{wp} = 11.7 and χ^2 = 4.37). Any effort to force the fits between calculated and experimental intensities for 222 peak causes large mismatch for other perovskite reflections leading to still higher χ^2 (= 4.85). The full pattern Rietveld fit for the composition with x=0.10 using *R*3*c* space group is shown in Fig. 4.5 (b). We can easily see from Fig. 4.5 that the rhombohedral model with *R*3*c* space group gives large mismatch between experimental

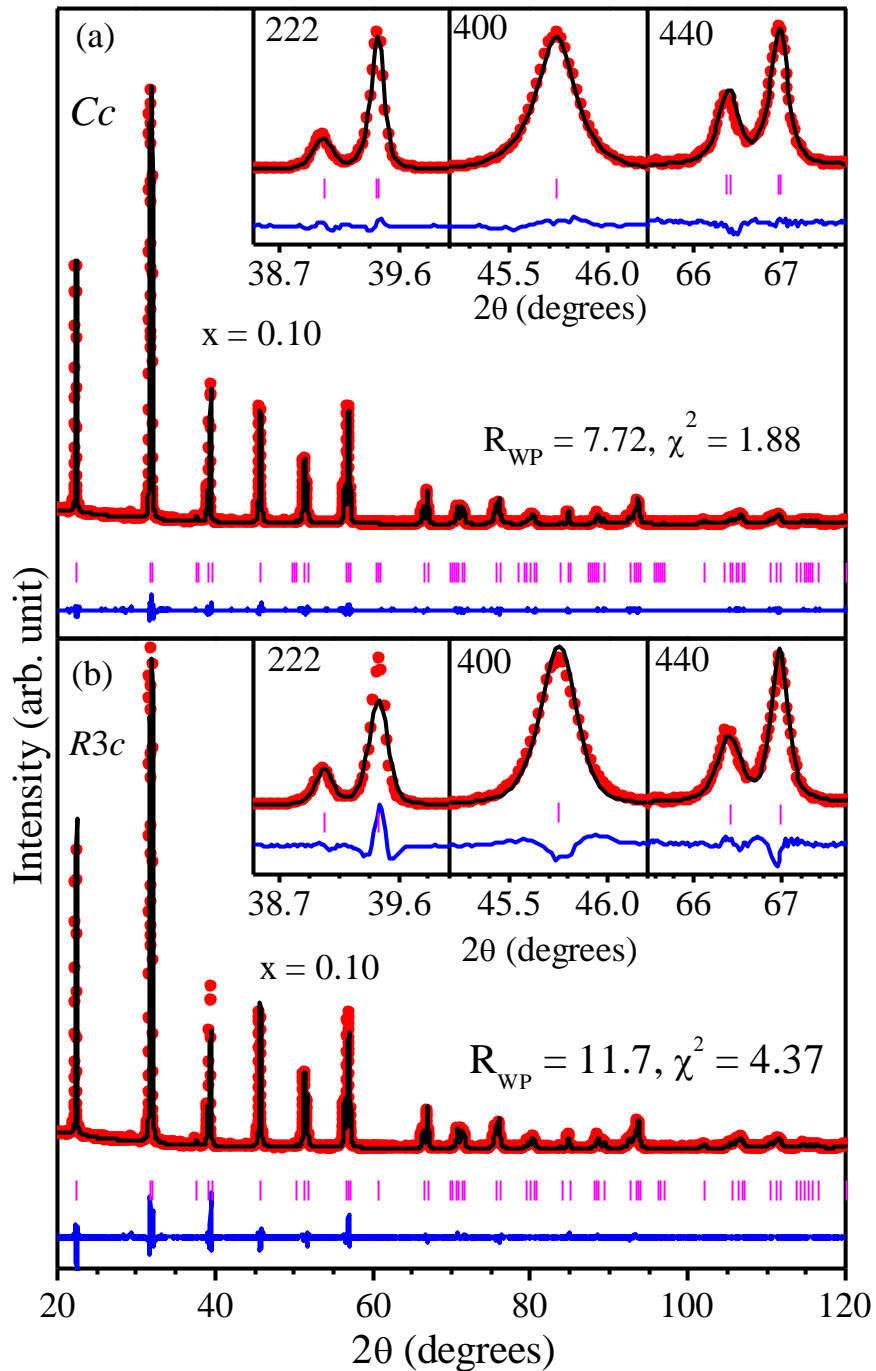and calculated diffraction profiles as compared to monoclinic structure with *Cc* space group.

Figure 4.5 The experimentally observed (dots), Rietveld calculated (overlapping continuous plot) and difference XRD profiles (bottom curve) obtained after Rietveld structural analysis by using (a) *Cc* space group and (b) *R3c* space group for (1-x)BiFeO$_3$-xSr(Fe$_{0.5}$Nb$_{0.5}$)O$_3$ ceramic with x = 0.10. The vertical tick marks above the difference profile represent the position of Bragg's reflections. The inset to (a) and (b) represent the zoomed portion of Rietveld fits of respective diffraction patterns.

Thus, the correct crystal structure of 0.90BF-0.10SFN ceramic is monoclinic with Cc space group. The structure Rietveld refinement for the composition with x = 0.15 was performed in a similar way as for x = 0.10, using monoclinic Cc space group. A very good fit is obtained for this composition also, as shown in Fig.4.6, which confirms the monoclinic structure. The refined structural parameters for the both the compositions x=0.10 and 0.15 having monoclinic structure with Cc space group are given in the Table 4.1.
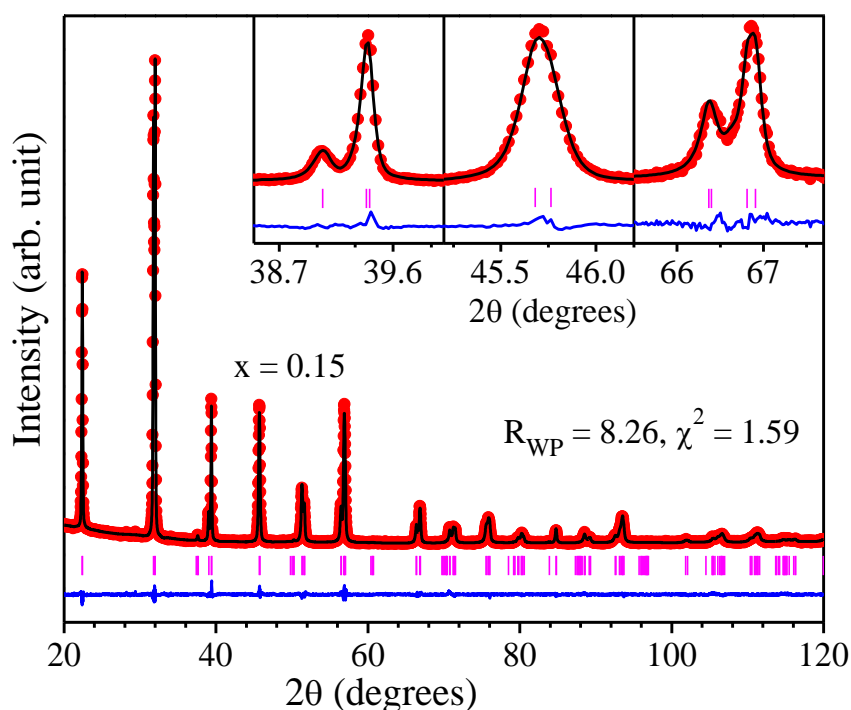

Figure 4.6 The experimentally observed (dots), Rietveld calculated (overlapping continuous plot) and difference XRD patterns (bottom curve) obtained after Rietveld structural analysis by using Cc space group for $(1-x)BiFeO_3-xSr(Fe_{0.5}Nb_{0.5})O_3$ ceramic with x = 0.15. The vertical tick marks above the difference profile represent position of Bragg's reflections. The inset depicts the zoomed portion of diffraction pattern for Rietveld fits.

4.4.3 Rietveld Structure Refinement of (1-x)BiFeO$_3$-xSr(Fe$_{0.5}$Nb$_{0.5}$)O$_3$ for 0.15 < x < 0.33 (Phase Coexistence of Monoclinic (*Cc*) and Cubic (*Pm-3m*) Structures)

Based on our qualitative analysis on the structure of (1-x)BF-xSFN from the evolution of the x-ray diffraction profiles with composition (x) discussed in section 4.4.1, coexistence of monoclinic and cubic structures is revealed for the composition range 0.15 < x < 0.33. Since the superlattice reflection, which is the characteristic of the existence of *Cc* phase in the coexisting region was found up to x = 0.30 (see Fig. 4.3), the first phase is taken as monoclinic with *Cc* space group as confirmed earlier and the second phase is considered as cubic with *Pm-3m* space group based on the singlet nature of the x-ray diffraction profiles. The Rietveld fit of full pattern x-ray diffraction profile for the 0.75BF-0.25SFN composition using coexistence of *Cc* and *Pm-3m* structures is shown in the Fig. 4.7. The overall fits between the experimentally observed and Rietveld calculated XRD patterns are quite satisfactory. During the structure refinement of x = 0.20 and 0.25 compositions, isotropic thermal parameters of the ions (for x = 0.20, Bi^{3+}/Sr^{2+} ≈ 0.87 & Fe^{3+}/Nb^{5+} ≈ 0.15 and for x =0.25, Bi^{3+}/Sr^{2+} ≈ 0.89 & Fe^{3+}/Nb^{5+} ≈ 0.18) in the monoclinic phase were found to be less than 1 and hence they were taken. However, the isotropic thermal parameters of the A-site ions in the monoclinic phase for x = 0.30 composition were found to be greater than 1 (Bi^{3+}/Sr^{2+} ≈ 1.98) and therefore, anisotropic thermal parameters were used for Bi/Sr ions. Since cubic symmetry (*Pm-3m*) only allows spherical symmetric vibrations of atom, in spite of high value of thermal parameters they were taken as isotropic. Inclusion of anisotropic thermal parameter for the monoclinic phase of x = 0.30 composition improved the fit between experimental and calculated x-ray diffraction patterns. The Rietveld refined structural and statistical parameters of (1-x)BF-xSFN ceramics for the compositions with x = 0.10, 0.15, 0.20, 0.25 and 0.30 are given in the Table 4.1.
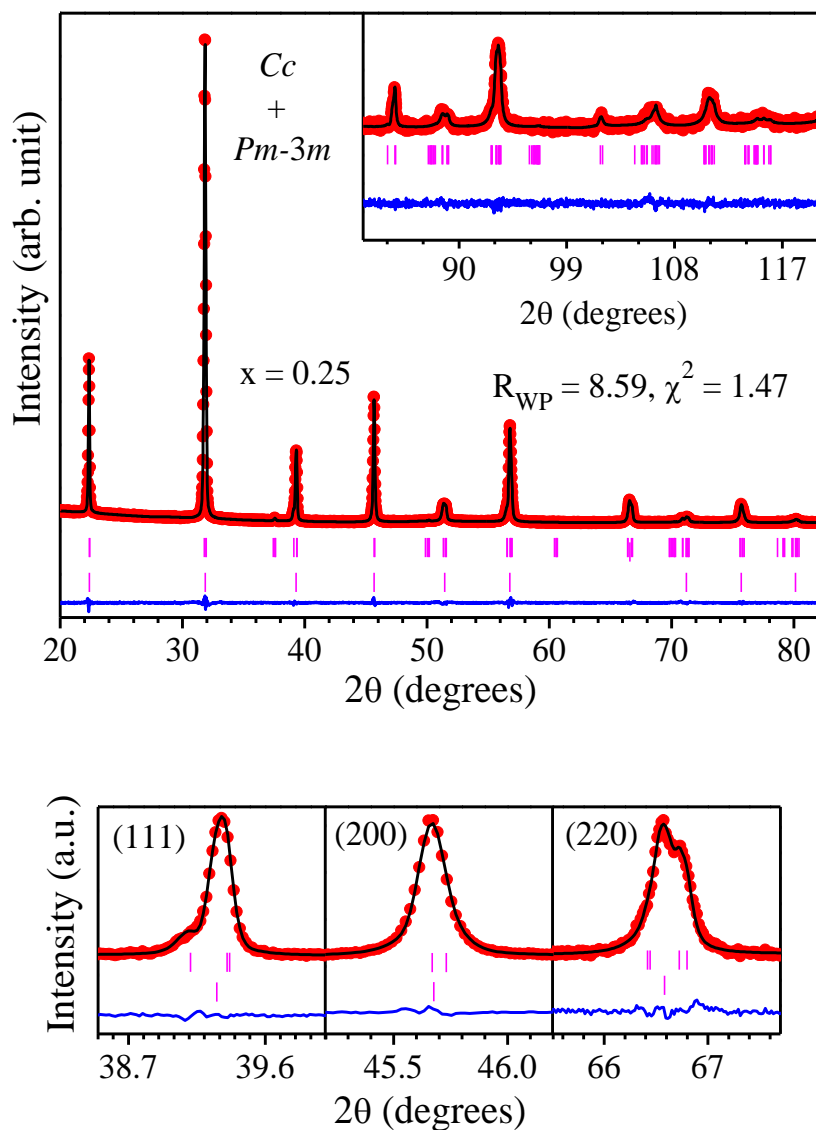
Figure 4.7 The experimentally observed (dots), Rietveld calculated (overlapping continuous plot) and difference XRD profiles (bottom curve) obtained after Rietveld structural analysis by using $Cc + Pm$-$3m$ space group for $(1-x)BiFeO_3$-$xSr(Fe_{0.5}Nb_{0.5})O_3$ ceramic with x=0.25. The lower panel shows the goodness of fits for zoomed pseudocubic perovskite peaks (111), (200) and (220) which clearly reveals the phase coexistence. The upper and lower vertical tick marks over the difference profile represent positions of Bragg's reflections corresponding to Cc and Pm-$3m$ space group respectively.

Table 4.1 Rietveld refined structural parameters for $(1-x)BiFeO_3-xSr(Fe_{0.5}Nb_{0.5})O_3$ ceramic with x = 0.10, 0.15, 0.20, 0.25 and 0.30. Positional coordinates are for monoclinic Cc space group.

x	0.1	0.15	0.20	0.25	0.30
Space group	*Cc*	*Cc*	*Cc* + *Pm-3m*	*Cc* + *Pm-3m*	*Cc* + *Pm-3m*
a	9.7716(5)	9.7647(3)	9.7604(3) 3.9676(4)	9.7533(2) 3.96915(2)	9.7274(4) 3.9690(2)
b	5.5844(4)	5.5965(5)	5.6004(6) 3.9676(4)	5.6028(7) 3.96915(3)	5.6068(2) 3.9690(2)
c	5.6298(1)	5.6298(2)	5.6284(7) 3.9676(4)	5.6258(1) 3.96915	5.6128(5) 3.9690(2)
β	125.76(6)	125.75(5)	125.67 (3)	125.61(5)	125.21(4)
$(Bi^{3+}/Sr^{2+})x$	0.00	0.00	0.00	0.00	0.00
$(Bi^{3+}/Sr^{2+})y$	0.25	0.25	0.25	0.25	0.25
$(Bi^{3+}/Sr^{2+})z$	0.00	0.00	0.00	0.00	0.00
$(Fe^{3+}/Nb^{5+})x$	0.225(6)	0.231(4)	0.233(2)	0.233(4)	0.238(5)
$(Fe^{3+}/Nb^{5+})y$	0.259(9)	0.241(8)	0.249(9)	0.247(8)	0.246(3)
$(Fe^{3+}/Nb^{5+})z$	0.782(3)	0.786(3)	0.783(2)	0.777(4)	0.745(7)
(O1)x	-0.027(8)	-0.031(6)	0.003(8)	0.004(6)	0.018(8)
(O1)y	0.187(4)	0.187(6)	0.184(6)	0.196(9)	0.299(5)
(O1)z	0.581(3)	0.524(7)	0.469(5)	0.463(7)	0.524(3)
(O2)x	0.214(9)	0.180(6)	0.211(6)	0.219(4)	0.332(6)
(O2)y	0.549(4)	0.528(5)	0.479(7)	0.478(2)	0.523(7)
(O2)z	0.037(5)	-0.013(7)	0.071(9)	0.081(4)	0.102(7)
(O3)x	0.243(9)	0.237(2)	0.266(5)	0.268(8)	0.324(6)
(O3)y	0.047(7)	0.037(5)	0.066(6)	0.062(7)	-0.027(3)
(O3)z	0.107(3)	0.083(6)	0.141(3)	0.143(5)	0.054(7)
R_{WP}	7.72	8.26	8.65	8.69	10.5
χ^2	1.88	1.60	1.56	1.52	1.37

4.4.4 Rietveld Structure Refinement of $(1-x)BiFeO_3-xSr(Fe_{0.5}Nb_{0.5})O_3$ for $0.33 \leq x \leq 0.70$ (Cubic (Pm-$3m$) Structure)

As discussed in section 4.4.1, all the pseudocubic XRD profiles shown in Fig. 4.1 are singlet, for $(1-x)BiFeO_3-xSr(Fe_{0.5}Nb_{0.5})O_3$ ceramic in the composition range $0.33 \leq x \leq 0.70$ suggesting cubic structure. The complete x-ray powder diffraction pattern in the two theta range 20 to 120° also shows the absence of any splitting or superlattice reflections for this composition range. Thus the structures in this composition range were refined considering cubic Pm-$3m$ space group. Fig. 4.8 (a) and (b) depict the experimentally observed, Rietveld calculated and difference XRD profiles in the 2θ range 20^0 to 120^0 for two selected compositions with x = 0.33 and 0.60, respectively. As can be seen from these figures the Rietveld fit is quite good confirming the cubic structure. Table 4.2 lists the refined structural parameters for the selected compositions in the range $0.33 \leq x \leq 0.70$. In the Rietveld structure refinement of cubic phase compositions, we have considered only isotropic thermal parameters. The isotropic thermal parameters of A and/or O-sites ions are very high (B_{iso} = 4.57(3) and 3.1(5) for A and O sites for x = 0.33) and the use of anisotropic thermal parameters in the cubic structure did not improve the agreement factors. This is because in the cubic symmetry, the thermal vibration of atoms is spherical for the A-site cations ($\beta_{11} = \beta_{22} = \beta_{33} = 0.074(3)$). The thermal parameters of oxygen are also nearly isotropic ($\beta_{11} = \beta_{22} = 0.094(3)$, $\beta_{33} = 0.089(7)$) within the limits of standard deviation even if the cubic structure model allows for anisotropy. All the compositions of the cubic phase region are refined well by considering the Pm-$3m$ model. The unusually large values of isotropic thermal parameters for Bi^{3+}/Sr^{2+} and O^{2-} ions indicate that these ions are locally displaced from their ideal cubic positions indicative of large local disorder in the crystal structure of $(1-x)BF-xSFN$ for $0.33 \leq x \leq 0.70$ compositions.
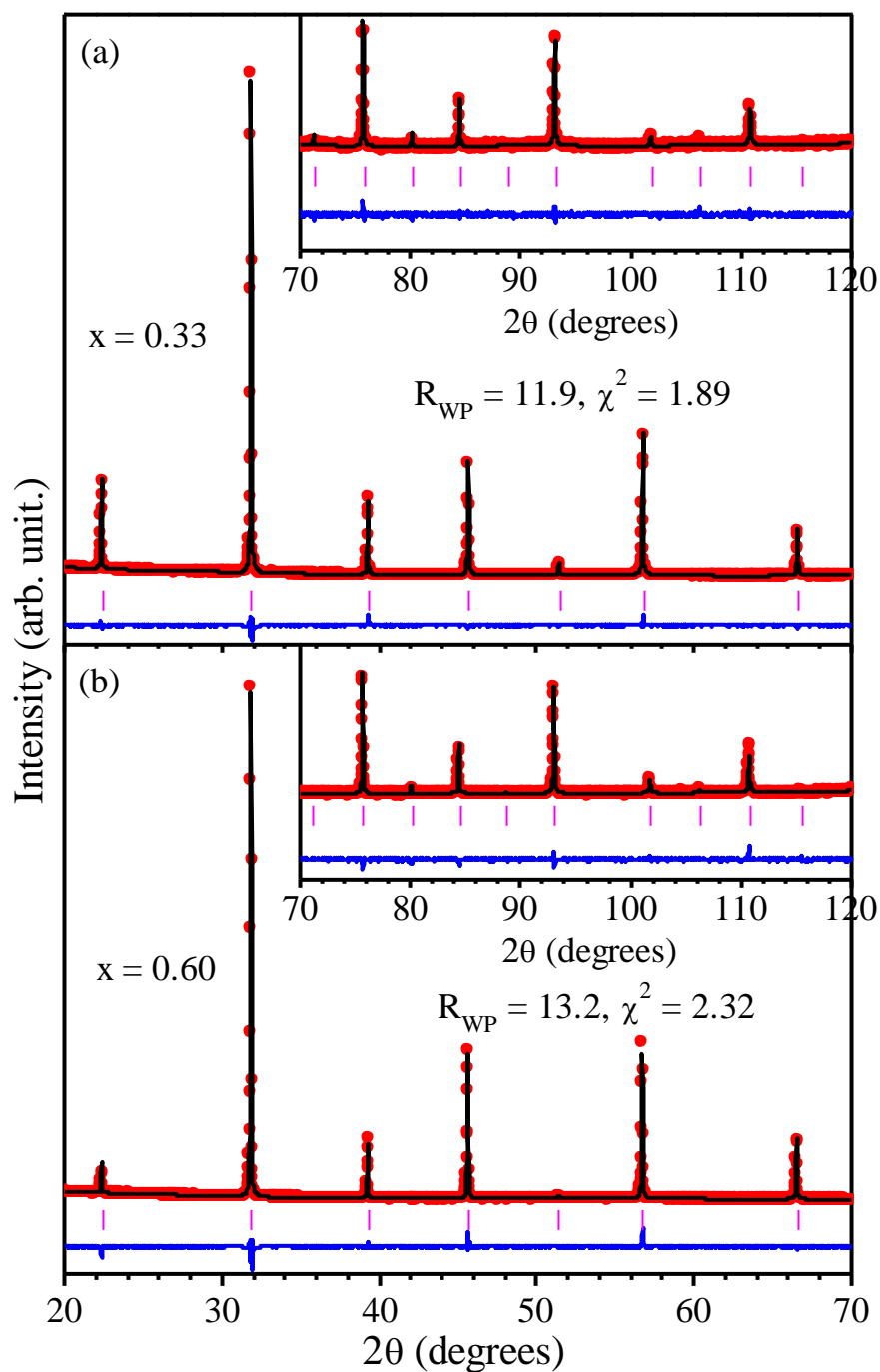
Figure 4.8 Experimentally observed (dots), Rietveld calculated (overlapping continuous plot) and difference XRD profiles (bottom curve) obtained after Rietveld structural analysis using *Pm*-3*m* space group for $(1-x)BiFeO_3-xSr(Fe_{0.5}Nb_{0.5})O_3$ ceramic with (a) x = 0.30 and (b) x = 0.60 compositions. The vertical tick marks above the difference profile represent position of Bragg's reflections. The inset indicates the zoomed portion in the 2θ range of 70-120°.

Table 4.2 Rietveld structural parameters for $(1-x)BiFeO_3-xSr(Fe_{0.5}Nb_{0.5})O_3$ ceramic with x = 0.33, 0.40, 0.50, 0.60 and 0.70.

x	0.33	0.40	0.50	0.60	0.70
Space group	*Pm-3m*	*Pm-3m*	*Pm-3m*	*Pm-3m*	*Pm-3m*
a = b = c	3.9694(4)	3.9713(5)	3.9716(3)	3.9719(1)	3.9717(2)
(Bi^{3+}/Sr^{2+})x,y,z	0.00	0.00	0.00	0.00	0.00
(Fe^{3+}/Nb^{5+})x,y,z	0.50	0.50	0.50	0.50	0.50
(O^{2-})x,y	0.50	0.50	0.50	0.50	0.50
(O^{2-})z	0	0	0.00	0.00	0.00
R_{WP}	11.9	11.1	11.5	13.2	14.5
χ^2	1.89	1.81	1.97	2.32	1.52

4.4.5 Rietveld Structure Refinement of $(1-x)BiFeO_3-xSr(Fe_{0.5}Nb_{0.5})O_3$ for $0.70 < x < 0.90$ (Phase Coexistence of Cubic (*Pm-3m*) and Tetragonal (*I4/mcm*) Structures)

As discussed earlier in section 4.4.1 for the compositions on the SFN end of $(1-x)BiFeO_3-xSr(Fe_{0.5}Nb_{0.5})O_3$, decreasing concentration of SFN ($0.70 < x < 0.90$) results in gradual reduction in the intensity of superlattice reflection as well as the tetragonal (*I4/mcm*) splitting in the XRD profiles. The structure finally transforms to cubic phase for x = 0.70 composition. A phase coexistence of tetragonal (space group *I4/mcm*) and cubic (space group *Pm-3m*) structures is evidenced for the composition range $0.75 \leq x \leq 0.85$. The Rietveld structure refinement of (1-x)BF-xSFN for the composition range $0.75 \leq x \leq 0.85$ indeed confirms the coexistence of tetragonal (space group *I4/mcm*) and cubic (space group *Pm-3m*) structures and excellent match between the Rietveld calculated and experimentally observed XRD patterns are obtained. The full pattern

Rietveld fit in the 2θ range 20^0 to 120^0 for a representative composition with x = 0.80 is depicted in Fig. 4.9.
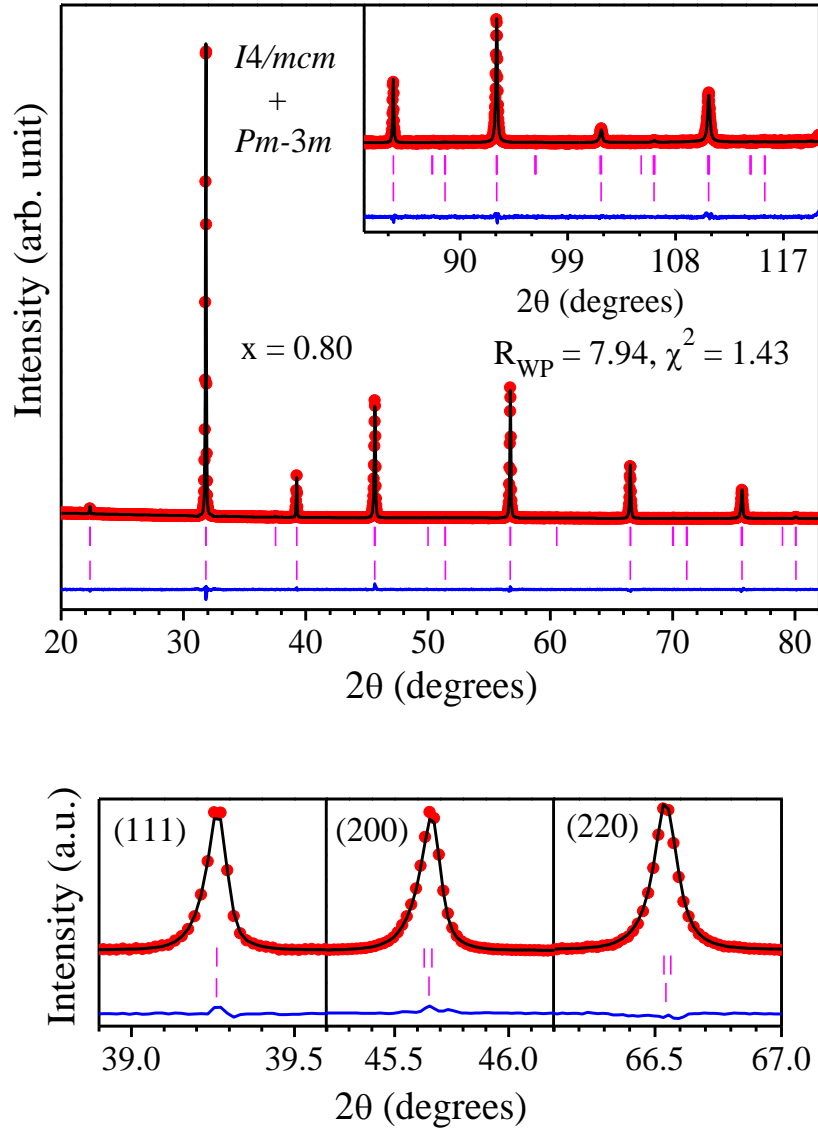

Figure 4.9 The experimentally observed (dots), calculated (solid line) and difference profiles (bottom solid line) obtained after Rietveld structural analysis by using *I4/mcm* + *Pm-3m* space group for (1-x)BiFeO$_3$-xSr(Fe$_{0.5}$Nb$_{0.5}$)O$_3$ ceramic with x=0.80. The lower panel shows the fits for zoomed perovskite peaks (111), (200) and (220). The upper and lower vertical tick marks over the difference profile represent position of Bragg's reflections corresponding to *I4/mcm* and *Pm-3m* space groups, respectively.

Consideration of a single phase tetragonal structure with *I4/mcm* space group does not fit well the experimental XRD pattern. Refined structural parameters for the composition range $0.75 \leq x \leq 0.85$ are listed in Table 4.3 (b). In spite of very high value of isotropic thermal parameters for A, B and O-site atoms (for x = 0.80, Bi/Sr = 10.7(1), Fe/Nb = 5.3(3) and O = 3.2(5)) in cubic phase, they were considered isotropic for the reasons explained in the previous section 4.4.4.

4.4.6 Rietveld Structure Refinement of $(1-x)BiFeO_3-xSr(Fe_{0.5}Nb_{0.5})O_3$ for x = 0.90 and 1.00 (Tetragonal (*I4/mcm*) Structure)

As discussed in Chapter 3, the structure of pure SFN (x=1) is tetragonal in the *I4/mcm* space group. As shown in Fig.4.1 and discussed in section 4.4.1, the nature of diffraction profiles for the composition with x=0.90 is also similar to that for pure SFN. This indicates the structure of the composition with x=0.90 is also likely to be tetragonal in the *I4/mcm* space group. The clear tetragonal splitting of 400 and 440 peaks, singlet appearance of 222 and 444 reflections (Fig. 4.1) along with the appearance of superlattice reflection at $2\theta \sim 37.5^0$ (Fig. 4.4) confirms the tetragonal structure for x=0.90 also. In view this, we performed the Rietveld structure refinement for x = 0.90 composition by considering *I4/mcm* space group. Fig. 4.10 depicts the experimentally observed, Rietveld calculated and difference XRD profiles for x=0.90 in the 2θ range 20^0 to 120^0. The Rietveld fit is very good with satisfactory values of statistical factors R_{wp} = 10.50 and χ^2 = 2.06, which confirms the single phase tetragonal structure with *I4/mcm* space group for x=0.90 also. Table 4.3 (b) lists the structural parameters obtained from the Rietveld refinement. The coordinates of the ions given in this table are for tetragonal phase. The values of isotropic thermal parameters for all the ions were found to be less than unity.
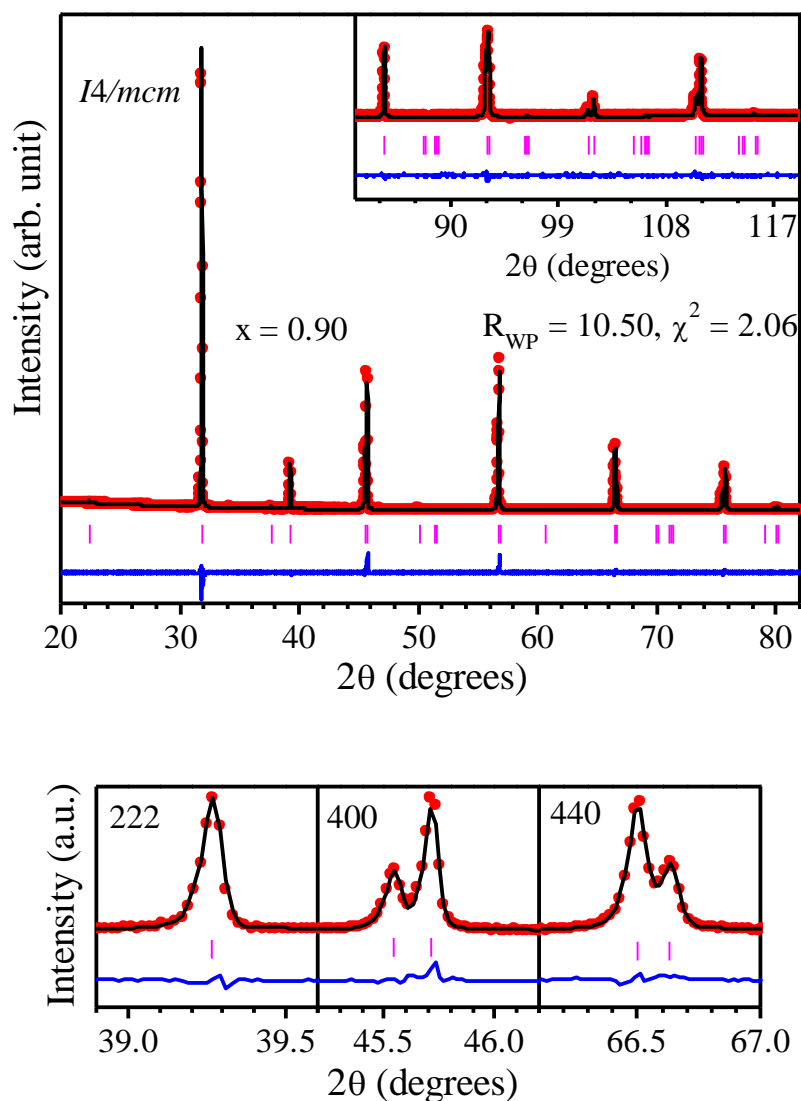
Figure 4.10 The experimentally observed (dots), Rietveld calculated (overlapping continuous plot) and difference XRD profiles (bottom curve) obtained after Rietveld structural analysis using *I4/mcm* space group for $(1-x)BiFeO_3-xSr(Fe_{0.5}Nb_{0.5})O_3$ ceramic with x=0.90. The lower panel show the zoomed Rietveld fits for the (222), (400) and (440) XRD profiles. The vertical tick marks above the difference profile represent positions of Bragg's reflections.

Table 4.3(a) Evolution of cubic phase fraction (%) with composition (x).

Composition (x)	0.10 to 0.15	0.20	0.25	0.30	0.33 to 0.70	0.75	0.80	0.85	0.9 to 1.0
Cubic fraction (%)	0.0	19.79	44.68	74.24	100	60.65	35.13	13.32	0.0

Table 4.3 (b) Rietveld refined structural parameters for $(1-x)BiFeO_3-xSr(Fe_{0.5}Nb_{0.5})O_3$ ceramic with x = 0.75, 0.80, 0.85, 0.90 and 1.00. The positional coordinates of the ions are for the tetragonal phase.

x	0.75	0.80	0.85	0.90	1.00
Space group	*I4/mcm* + *Pm-3m*	*I4/mcm* + *Pm-3m*	*I4/mcm* + *Pm-3m*	*I4/mcm*	*I4/mcm*
a	5.6155(6) 3.9714(2)	5.6147(4) 3.9713(7)	5.6114(3) 3.9705(9)	5.6099(1)	5.6086(8)
b	5.6155(6) 3.9714(2)	5.6147(4) 3.9713(7)	5.6114(3) 3.9705(9)	5.6099(1)	5.6086(8)
c	7.9445(4) 3.9714(2)	7.9462(3) 3.9713(7)	7.9545(4) 3.9705(9)	7.9617(3)	7.9713(3)
$(Bi^{3+}/Sr^{2+})x$	0.00	0.00	0.00	0.00	0.00
$(Bi^{3+}/Sr^{2+})y$	0.50	0.50	0.50	0.50	0.50
$(Bi^{3+}/Sr^{2+})z$	0.25	0.25	0.25	0.25	0.25
$(Fe^{3+}/Nb^{5+})x,y,z$	0.00	0.00	0.00	0.00	0.00
(O1)x,y	0.00	0.00	0.00	0.00	0.00
(O1)z	0.25	0.25	0.25	0.25	0.25
(O2)x	0.2346(5)	0.2307(8)	0.2262(7)	0.2278(5)	0.2229(6)
(O2)y	0.7346(5)	0.7307(8)	0.7262(8)	0.7278(5)	0.7229(6)
(O2)z	0.00	0.00	0.00	0.00	0.00
R_{WP}	9.20	11.1	8.33	10.5	12
χ^2	1.58	1.81	1.65	2.06	2.52

4.4.7 Composition Dependent Variation of Lattice Parameters and Unit Cell Volume for $(1-x)BiFeO_3-xSr(Fe_{0.5}Nb_{0.5})O_3$ Ceramic

Fig. 4.11(a) depicts the composition dependent variation of pseudocubic lattice parameters for (1-x)BF-xSFN ceramics in the composition range $0.10 \leq x \leq 1.00$. The

vertical lines drawn in Fig. 4.11 demarcate the stability region of various crystallographic phases. The lattice parameters were scaled suitably to compare with the primitive perovskite cell for examining the composition dependence. The pseudocubic lattice parameters a_p, b_p and c_p for monoclinic cell was obtained by using $a_p \approx a/\sqrt{6}$, $b_p \approx b/\sqrt{2}$ and $c_p \approx c/\sqrt{2}$ relationship where a, b and c are lattice parameters corresponding to monoclinic cell while pseudocubic cell parameters for the tetragonal phase in *I4/mcm* space group was obtained by using $a_p = b_p \approx a_t/\sqrt{2}$ and $c_p \approx c_t/2$, relationship where a_t and c_t are lattice parameters corresponding to tetragonal cell in *I4/mcm* space group. The pseudocubic lattice parameters a_p and c_p for the monoclinic phase decrease up to x = 0.25, the rate of decrease for a_p is more than c_p, and then there is a sharp fall in both for x = 0.30. The pseudocubic b_p parameter of the monoclinic phase increases continuously and approaches to the lattice parameter corresponding to the cubic phase with $x_c = 0.33$. The sharp fall in the values of a_p and c_p from x = 0.25 to x = 0.30 means a significantly large reduction in the monoclinic distortion of the unit cell due to onset of monoclinic to cubic phase transformation at the phase boundary. This is also confirmed by the appearance of very small intensity superlattice reflection in the diffraction pattern [see inset to Fig. 4.3 (b)]. After x = 0.30 composition both a_p and c_p approach to the value of cubic lattice parameter for the critical composition $x_c = 0.33$. The monoclinic to cubic phase transition occurs over a composition range of 0.15 < x < 0.33 where both the phases coexist. In the cubic phase region $0.33 \leq x \leq 0.70$ the lattice parameter is nearly composition independent. Above x = 0.70 composition second phase coexistence region starts with the coexistence of tetragonal and cubic phases. The pseudocubic lattice parameters a_p and c_p corresponding to the tetragonal phase show departure from each other due to enhancement of the tetragonality with increasing the concentration of the SFN.
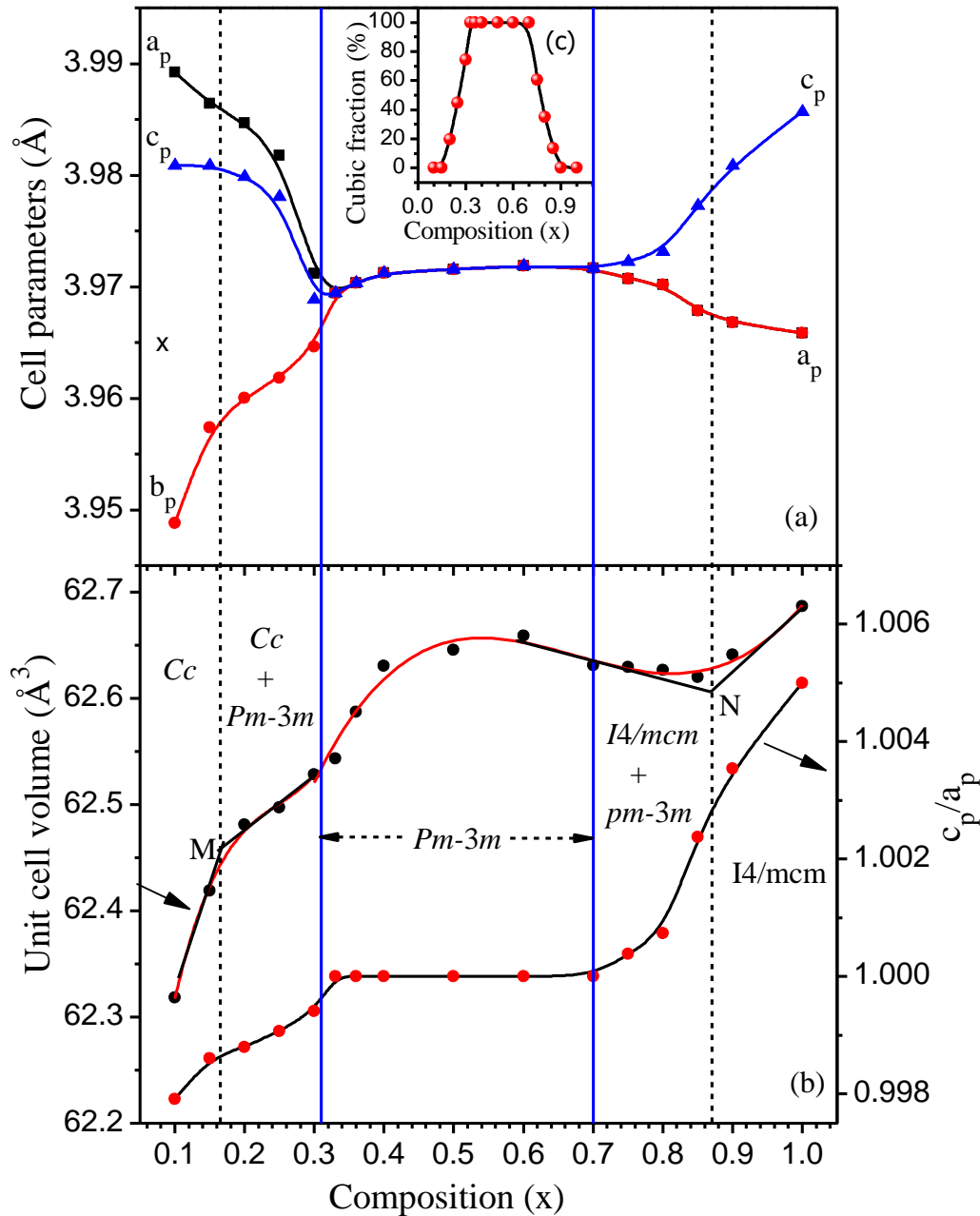
Figure 4.11 Composition variation of (a) refined pseudocubic lattice parameters a_p, b_p and c_p (b) pseudocubic unit cell volume (left axis scale) and ratio of c_p to a_p (right axis scale) for $(1-x)BiFeO_3-xSr(Fe_{0.5}Nb_{0.5})O_3$ ceramic (c) evolution of cubic fraction (*Pm-3m*) (%) with composition (x). Dots represent the experimental data while continuous lines are guide to eyes.

The variations of unit cell volume (left scale) and the ratio of pseudocubic lattice parameter c_p to a_p (right scale) are depicted in Fig. 4.11 (b). The solid line that follows the variation of unit cell volume with composition is generated from the

polynomial fits of experimental data points. The unit cell volume for monoclinic phase increases with the composition (x) and shows an anomaly in between x = 0.30 and 0.33 which is experimentally observed phase boundary for the monoclinic to cubic phase transition. To estimate the composition where this phase transition begins, we have drawn two tangents, on the composition variation of unit cell volume, crossing at point M. The point M corresponds to the composition x ~ 0.17. This is the value of composition (x) below which (1-x)BF-xSFN ceramic has stable monoclinic structure while above this (x) value cubic phase becomes stable leading to phase coexistence. On entering in the cubic phase region unit cell volume continues to increase to attain a maximum value for the composition x ≈ 0.60 and then start to decrease slowly up to x = 0.85. The crossing point N of two tangents drawn on the composition dependence of unit cell volume on the SFN end corresponds to the x = 0.87. This is the value of composition (x) below which two phases (*I4/mcm* + *Pm-3m*) coexist and above this value only tetragonal phase persists. For the compositions with x>0.87, tetragonality [i.e. ratio of c_p to a_p] as well as unit cell volume enhance significantly with increasing (x) in the tetragonal phase region. The enhancement of the unit cell volume with increasing the value of SFN concentration (x) for (1-x)BF-xSFN ceramic is attributed to the substitution of bigger Sr^{2+} (1.44 Å) and Nb^{5+} (0.64 Å) ions at the smaller Bi^{3+} (1.11 Å) and Fe^{3+} (0.55 Å) sites, respectively [Shannon and Prewitt (1969)]

4.4.8 Composition Dependence of Room Temperature Dielectric Permittivity

Fig. 4.12 shows the variation of dielectric permittivity as a function of composition (x) for (1-x)BF-xSFN ceramic at room temperature at three measuring frequencies 100kHz, 300kHz and 1MHz. The value of dielectric permittivity is presented by dots in Fig. 4.12 while continuous line is guide to eyes. As expected the

dielectric permittivity decreases with increasing frequency (ω) but appreciable permittivity with composition dependence similar to that for lower frequencies is seen at 1MHz also.
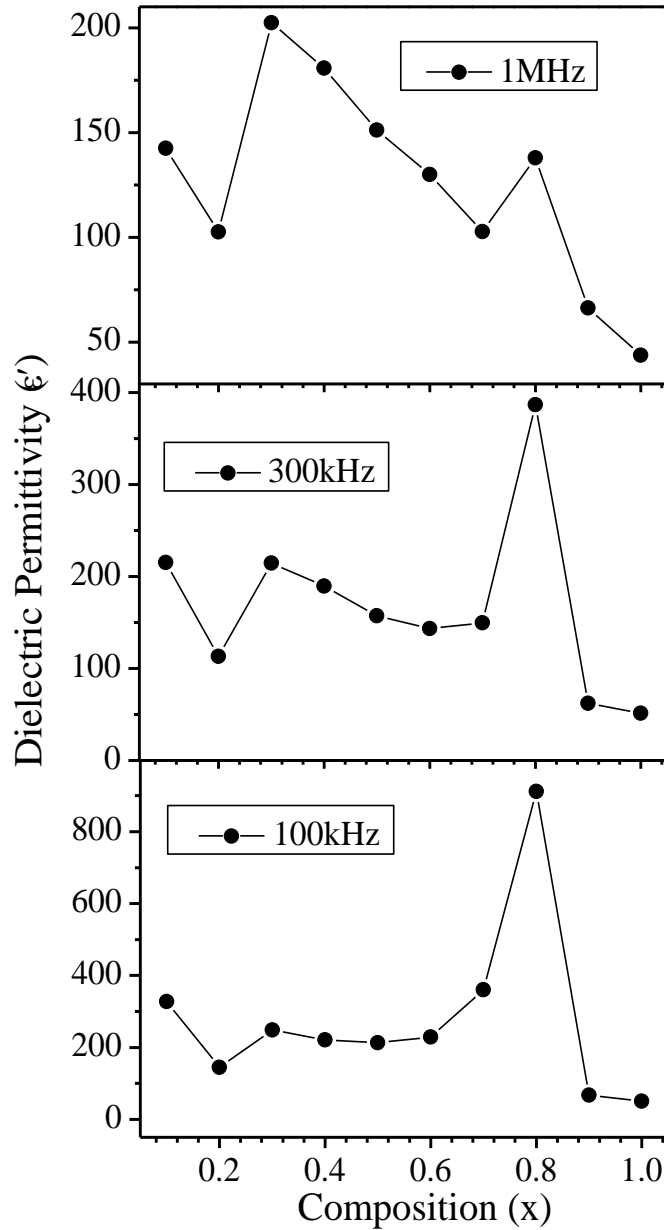

Figure 4.12 Composition dependent variation of dielectric permittivity (ε') for (1-x)BiFeO$_3$-xSr(Fe$_{0.5}$Nb$_{0.5}$)O$_3$ ceramic at room temperature. Dots are experimental values while line is guide to eyes.

This suggests that the dielectric permittivity for each composition of (1-x)BF-xSFN at 1MHz frequency nearly comes from the intrinsic contribution of grains only.

The variation of room temperature dielectric permittivity as the function of composition in Fig. 4.12 shows two peaks at x $\approx$ 0.30 and x $\approx$ 0.80, which are close to the crystallographic phase boundaries between monoclinic-cubic structures and cubic-tetragonal structures, respectively. In analogy to the $(1-x)BiFeO_3-xPb(Fe_{0.5}Nb_{0.5})O_3$ [Patel (2014)], $(1-x)BiFeO_3-xBaTiO_3$ [Singh et al. (2013)] and $Pb(Zr_xTi_{1-x}O_3$ [Jaffe (1971)] ceramic systems, where composition dependent dielectric permittivity marks peak at the compositions close to crystallographic phase boundary, (also popular as morphotropic phase boundary) the two peaks at x $\approx$ 0.30 and x $\approx$ 0.80 in dielectric permittivity versus composition (x) plot for (1-x)BF-xSFN ceramic system also correspond the morphotropic phase transitions. The two phase boundaries at x $\approx$ 0.30 and x $\approx$ 0.80 separate the stability regions of three crystallographic phase regions of $(1-x)BiFeO_3-xSr(Fe_{0.5}Nb_{0.5})O_3$ ceramic.

4.4.9 Temperature Dependent dc Magnetization M(T) Measurements on $(1-x)BiFeO_3-xSr(Fe_{0.5}Nb_{0.5})O_3$ Ceramics

The effect of solid solution formation of SFN with BF on the magnetic properties were investigated by studying temperature dependent dc magnetization M(T) measurements on various compositions above room temperature. The magnetic transition temperature and the nature of magnetic ordering in various compositions of (1-x)BF-xSFN ceramic has been investigated by dc magnetization M(T) measurement as a function of temperature above room temperature. Fig. 4.13 shows the variation of magnetization (M) with temperature for different compositions of (1-x)BF-xSFN ceramic. The value of magnetization (M) for the composition range $0.10 \leq x < 0.50$, initially increases with increasing temperature and after achieving a maximum value at a certain temperature; it starts to decrease and shows another magnetic anomaly at somewhat higher temperature.
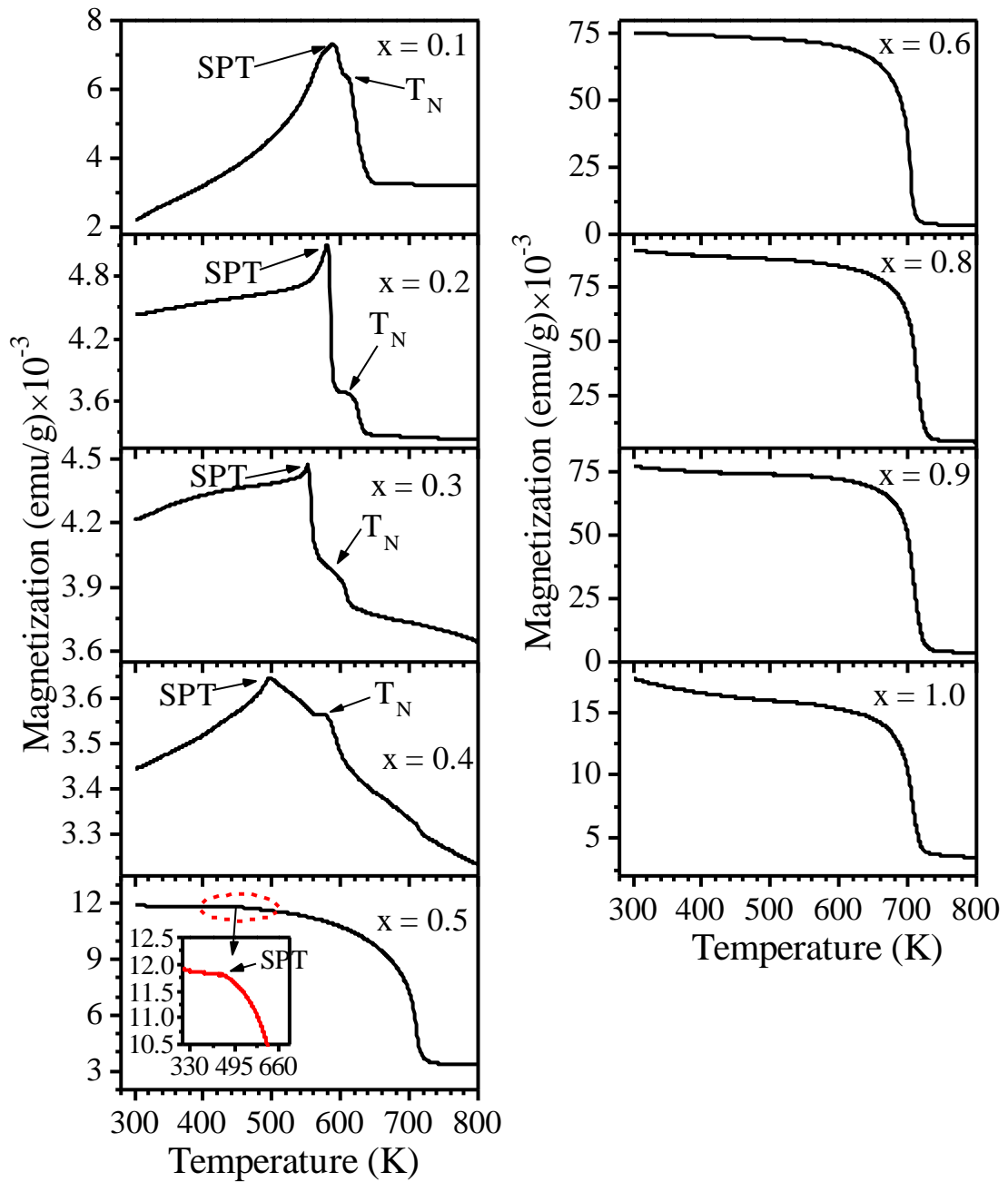
135

Figure 4.13 Temperature dependence of magnetization for various compositions of (1-x)BiFeO₃-xSr(Fe₀.₅Nb₀.₅)O₃ ceramic in the range $0.1 \leq x \leq 1.0$ measured at 500 Oe magnetic fields. T_N and SPT stand for antiferromagnetic and spin-reorientation phase transition temperatures, respectively.

In analogy to the magnetic transitions reported earlier for monoclinic (*Cc*) compositions of (1-x)BiFeO₃-xPbTiO₃ (x = 0.25 and 0.27) [Bhattacharjee et al. (2013)], the lower and higher temperature side magnetic anomalies in M(T) plot of Fig.

4.13 were considered as spin-reorientation phase transition (SPT) and antiferromagnetic phase transition (T_N) respectively. In addition to these two anomalies, a third one also appears for x = 0.40 composition around $\sim 705K$ temperature which resembles to the magnetic transition observed in higher compositions. In contrast, the nature of the M(T) plots for the compositions range $0.50 \leq x \leq 1.0$ are different from the lower composition values of 'x'. The M(T) plot for x = 0.50 composition show two magnetic anomalies around $\sim 455K$ (shown in the inset to x = 0.50 plot of Fig. 4.13) and $\sim 708K$ while the remaining compositions in the range $0.60 \leq x \leq 1.0$ show only one magnetic transition occurring around ~ 704 to $713K$. For these compositions, the magnetization (M) slowly decreases with the increase of temperature and show a strong drop in magnetization value at the transition temperature. The nature of magnetization curves M(T) for all these compositions (i.e. $0.50 \leq x \leq 1.0$) are found to be very similar except for x = 0.50, with a slight difference, that shows a magnetic anomaly at 455K. Such kind of M(T) behaviour is observed due to weak but dominant ferromagnetic contribution to the magnetization value which is recently reported by us for SFN ceramic also [Kumar and Singh (2019)], as discussed in Chapter 3. The disappearance of antiferromagnetic anomaly (T_N) of $BiFeO_3$ for x > 0.40 compositions suggests that the antiferromagnetic ordering of Fe^{3+} ions is destroyed for these compositions. However, the spin-reorientation phase transition anomaly persists up to x = 0.50 composition. Thus we can say that, the M(T) behaviour of (1-x)BF-xSFN ceramic is dominated by BF up to x < 0.5 and by SFN for $x \geq 0.50$ compositions. The variation of spin-reorientation phase transition (SPT) temperature and antiferromagnetic transition temperature (T_N) as a function of composition are shown in Fig. 4.14(a) and (b), respectively. Both the Neel temperature (T_N) and spin-reorientation phase transition (SPT) temperatures decrease with increasing concentration of SFN ceramic i.e. by

increasing the content of the non-magnetic (Nb^{5+}) ion at the B-site of the perovskite lattice as can be seen from Fig. 4.14. The decrease in antiferromagnetic transition temperature (T_N) with increasing concentration of SFN ceramic in $BiFeO_3$ matrix is attributed to the dilution of the magnetic sublattice of $BiFeO_3$ by the substitution of Nb^{5+} ions [Patel et al. (2013)].
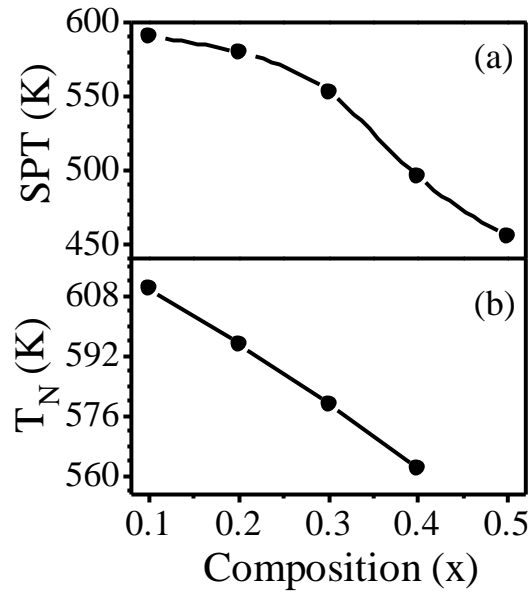

Figure 4.14 Composition dependence of (a) spin reorientation transition (SPT) temperature and (b) antiferromagnetic transition (T_N) temperature for $(1-x)BiFeO_3$-$xSr(Fe_{0.5}Nb_{0.5})O_3$ ceramic.

4.4.10 Magnetic Behaviour of $(1-x)BiFeO_3$-$xSr(Fe_{0.5}Nb_{0.5})O_3$ Ceramic at Room Temperature

As discussed in chapter 1, due to the presence of incommensurate and spatially modulated spiral spin structure with approximate periodicity of ~ 62nm, $BiFeO_3$ exhibits linear magnetization versus magnetic field hysteresis loop [Lebeugle et al. (2007)B]. The room temperature magnetization (M) versus applied magnetic field (H), in the range $\pm$ 50 kOe, plots for $(1-x)$BF-xSFN ceramic in the composition range $0.10 \leq x \leq 1.0$ are shown in Fig. 4.15, to investigate the effect of SFN substitution.
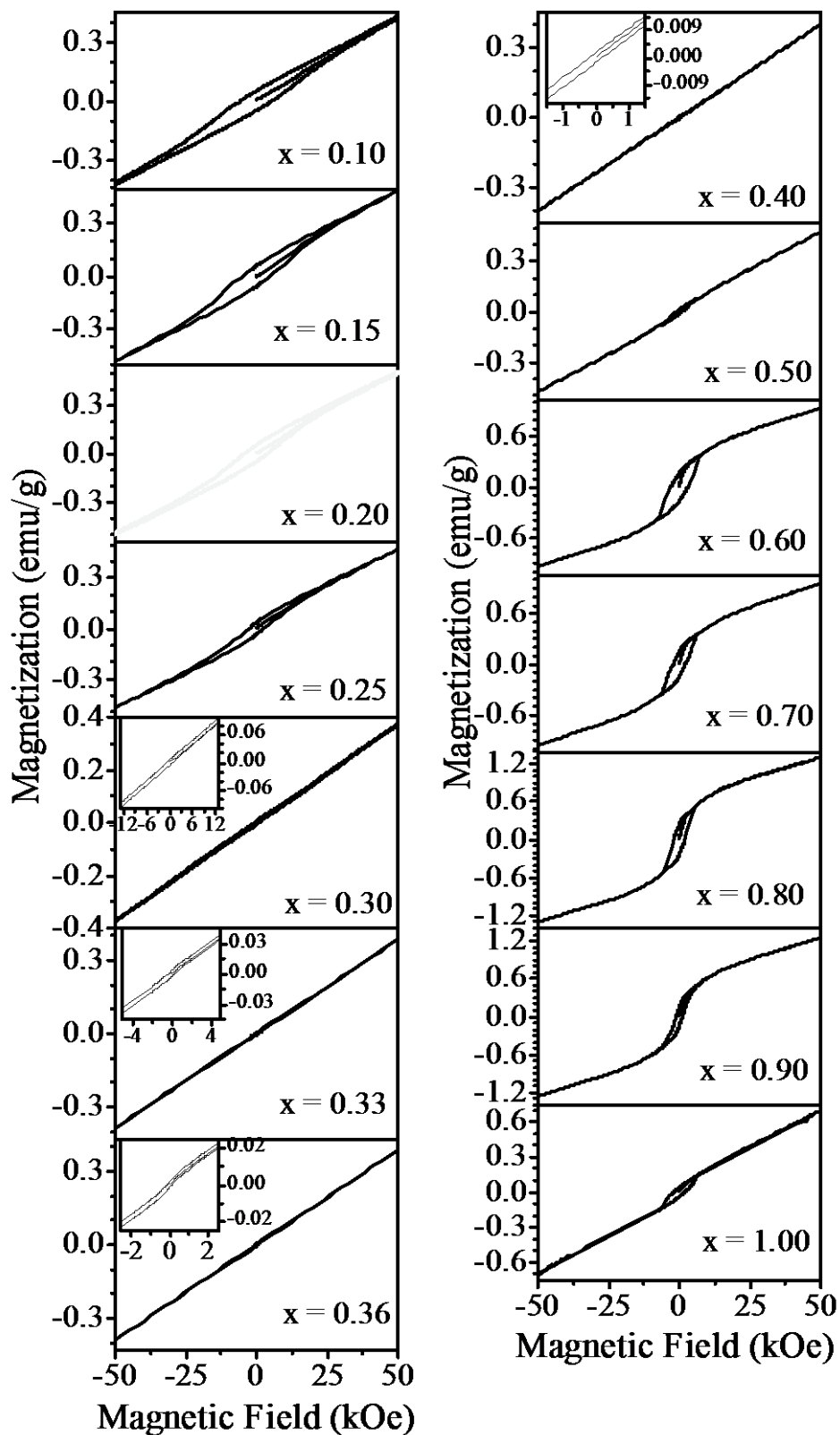
Figure 4.15 Magnetization versus (M) magnetic field (H) plot for various compositions of $(1-x)BiFeO_3-xSr(Fe_{0.5}Nb_{0.5})O_3$ ceramic.

All the compositions of (1-x)BF-xSFN ceramic show open M-H hysteresis loop. However, unlike the ferromagnetic materials, the hysteresis loops of BF-xSFN ceramic at room temperature do not show saturation of magnetization even after the application of high magnetic field of 5T. Instead, the magnetization varies linearly as a function of applied field that can be clearly observed from Fig. 4.15. This kind of behaviour of M-H response is attributed to the induction of weak ferromagnetism in canted antiferromagnetic systems [Serrao et al. (2005)]. As shown in Fig. 4.15, the remnant magnetization (Mr) initially increases with increasing composition (x) from zero value for $BiFeO_3$ to the maximum value (~ 0.0578 emu/g) for x = 0.15 after which it decreases with increasing x and attains a minimum value for x ~ 0.33. On increasing the SFN content (x) further, the Mr starts increasing and shows another peak at x ~ 0.80 (~ 0.23 emu/g) after which it starts decreasing up to x = 1.0. The value of Mr at the first peak, for x = 0.15 is found to be 0.25 times smaller than that at the second peak.

The induction of weak ferromagnetism in (1-x)BF-xSFN ceramic is the result of partial or complete destruction of the spiral spin structure of $BiFeO_3$ on $Sr(Fe_{0.5}Nb_{0.5})O_3$ substitution. It was found that the application of high magnetic field (H $\geq$ 20 Tesla) along $[001]_h$ direction of $BiFeO_3$ single crystal transforms spatially modulated spin cycloid of $BiFeO_3$ to a spatially homogeneous antiferromagnetic structure [Popov et al. (2001), Popov et al. (1993), Ruette et al. (2004)]. This kind of transformation in the spin structure of $BiFeO_3$ releases the latent magnetization, which was reported to be approximately ~ 0.3 emu/g at 10K [Wang et al. (2005)]. Substitution of $BiFeO_3$ by La^{3+} ions is reported to induce weak ferromagnetism in $Bi_{0.93}La_{0.07}FeO_3$ [Sosnowska et al. (1996)]. A remnant magnetization with Mr ~ 0.15 emu/g at 300K and ~ 0.3 emu/g at T = 5K have also been reported in the $(Bi_{0.8}La_{0.2})(Fe,Ga)O_3$-45%$PbTiO_3$ solid solution [Wang et al. (2005)]. The value of Mr ~ 0.3 emu/g reported at 5K in

$(Bi_{0.8}La_{0.2})(Fe,Ga)O_3\text{-}45\%PbTiO_3$ solid solution is comparable to the value of magnetization that is observed on the application of very high magnetic field (~ 20 T) to the pure $BiFeO_3$ at 10K. This suggests that the transformation of modulated spiral spin structure to homogenous spin structure can also be possible by chemical substitutions. The destruction of spiral spin structure in the $BiFeO_3$ based solid solutions was also confirmed by the analysis of neutron diffraction data of $Bi(Mn_{0.1}Fe_{0.9})O_3$ and $(Bi_{0.8}Ba_{0.2})(Fe_{0.8}Ti_{0.2})O_3$ [Sosnowska et al. (2002), Singh et al. (2011)]. Similarly, in $(1\text{-}x)BiFeO_3\text{-}xBaTiO_3$ ceramic system, remnant magnetization Mr ~ 0.05 emu/g for x = 0.10 [Singh et al. (2008)C] and ~ 0.15 emu/g for x = 0.20 has been reported [Singh et al. (2011)]. More recently, in 20% $CaTiO_3$ substituted $BiFeO_3$; the value of remnant magnetization was reported as Mr ~ 0.18 emu/g at 300K and ~ 0.26 emu/g at 5 K, respectively [Wang et al. (2012)].

In the present study, the Mr values in (1-x)BF-xSFN solid solutions in the composition range $0.10 \leq x \leq 0.50$ at room temperature is approximately three times lower than that reported due to the melting of the spiral spin structure of $BiFeO_3$ either by doping or by application of intense magnetic field (H ~ 20T) [Popov et al. (1993), Wang et al. (2005)]. However, the value of remnant magnetization at room temperature for compositions $0.50 < x \leq 0.90$ is found ($\sim 0.17\text{-} 0.23$ emu/g and ~ 0.15 emu/g for x = 0.9) very close to or greater than the reported values obtained for the 20% $CaTiO_3$ [Wang et al. (2012)] and 20% $BaTiO_3$ [Singh et al. (2011)] doped $BiFeO_3$ solid solutions. The composition dependent variation of remnant magnetization for (1-x)BF-xSFN ceramic system showing two peaks at $x \approx 0.15$ and $x \approx 0.80$ is depicted in Fig. 4.16. The observation of very low value of Mr in the composition range $0.10 \leq x \leq 0.50$ suggests that either the canting angle is very small or spiral spin structure of $BiFeO_3$ is only partially suppressed even with 50% substitution with SFN.
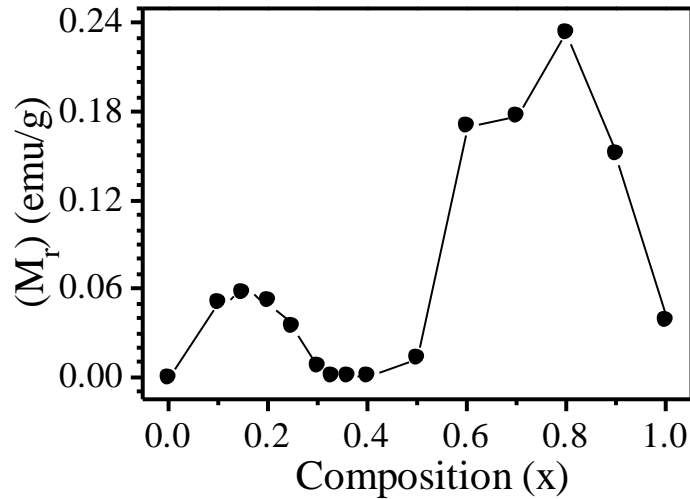
Figure 4.16 Composition dependence of remnant magnetization (M_r) for $(1-x)BiFeO_3$-$xSr(Fe_{0.5}Nb_{0.5})O_3$ ceramic.

While for higher compositions $0.50 < x \leq 0.90$, the higher value of Mr suggests that the spiral spin structure has been completely suppressed. Thus the appearance of remnant magnetization (either low or high) in $(1-x)BF-xSFN$ solid solution suggests that the $Sr(Fe_{0.5}Nb_{0.5})O_3$ substitution also transforms the modulated spiral spin structure of $BiFeO_3$ to partially or completely homogenous spin structure.

4.5 Conclusions

A comprehensive crystallographic and Rietveld structural analysis of x-ray diffraction data for the room temperature crystal structure of $(1-x)BF-xSFN$ solid solution reveals that a new monoclinic structure with space group *Cc* is observed for the composition range $0.1 \leq x \leq 0.15$. The monoclinic structure transforms to cubic structure with increasing the concentration of SFN in the solid solution. Coexistence of monoclinic (*Cc*) and cubic (*Pm-3m*) structure is obtained for the composition range $0.15 < x < 0.33$. The monoclinic (*Cc*) to cubic (*Pm-3m*) phase transition gets completed at $x_c \sim 0.33$. A single phase cubic structure with local disorder of A and B-site cations is observed for the intermediate composition range $0.33 \leq x \leq 0.70$ in $(1-x)BF-xSFN$ solid solution. Another phase coexistence region is observed for the composition range

0.70 < x ≤ 0.85 in which tetragonal structure with space group *I4/mcm* and cubic structure with space group *Pm-3m* are present. At SFN end, for the composition range 0.85 < x ≤ 1.00, the structure of (1-x)BF-xSFN is single phase tetragonal with *I4/mcm* space group. Composition dependent variation of dielectric permittivity shows two peaks around the compositions x ≈ 0.30 and x ≈ 0.80 for (1-x)BF-xSFN ceramic. Temperature dependent magnetization measurements on various compositions of (1-x)BF-xSFN ceramic reveals that the antiferromagnetic ordering of Fe^{3+} ions in $BiFeO_3$ is destroyed for the compositions with x>0.40. Both the Neel temperature (T_N) and spin-reorientation phase transition (SPT) temperatures decrease with increasing concentration of SFN ceramic for the compositions with x<0.50 due to dilution effect of Fe^{3+} ions. Investigation of magnetization (M)-applied magnetic field (H) hysteresis loops for the various composition of 1-x)BF-xSFN ceramic reveals induction of weak ferromagnetism in canted antiferromagnetic order of $BiFeO_3$ due to solid solution formation with SFN. The composition dependent variation of remnant magnetization for (1-x)BF-xSFN ceramic shows two peaks around x ≈ 0.15 and x ≈ 0.80. The non-zero value of remnant magnetization (Mr) obtained from M-H hysteresis loop of (1-x)BF-xSFN solid solution reveals that the $Sr(Fe_{0.5}Nb_{0.5})O_3$ substitution in $BiFeO_3$ transforms it's modulated cycloidal spin structure to a partially or completely homogenous spin structure.